JGR Atmospheres

RESEARCH ARTICLE
10.1029/2020JD032908

Corona Discharge in Wind for Electrically Isolated Electrodes

C. Guerra-Garcia[1], N. C. Nguyen[1], T. Mouratidis[1], and M. Martinez-Sanchez[1]

[1]Department of Aeronautics and Astronautics, Massachusetts Institute of Technology, Cambridge, MA, USA

Key Points:
- Classical scaling laws of corona discharge in wind do not apply for electrically isolated electrodes
- For electrically floating electrodes corona current can decrease in wind in response to charging
- Glow corona discharge in wind can be used for controlled charging of an electrically isolated body

Correspondence to:
C. Guerra-Garcia,
guerrac@mit.edu

Citation:
Guerra-Garcia, C., Nguyen, N. C., Mouratidis, T., & Martinez-Sanchez, M. (2020). Corona discharge in wind for electrically isolated electrodes. *Journal of Geophysical Research: Atmospheres*, *125*, e2020JD032908. https://doi.org/10.1029/2020JD032908

Received 10 APR 2020
Accepted 13 JUL 2020
Accepted article online 28 JUL 2020

Abstract For various problems in atmospheric electricity it is necessary to understand the behavior of corona discharge in wind. Prior work considers grounded electrode systems, of relevance for earthed towers, trees, or windmills subjected to thunderstorms fields. In this configuration, the effect of wind is to remove the shielding ions from the coronating electrode vicinity strengthening the corona and increasing its current. There are a number of cases, such as isolated wind turbine blades or airborne vehicles, that are not completely represented by the available models and experiments. This paper focuses on electrode systems that are electrically isolated from their environment and reports on a wind tunnel campaign and accompanying theoretical work. In this configuration, there are two competing effects: the removal of the shielding ions by the wind, strengthening the corona; and the electrode system charging negatively (for positive corona) with respect to its environment, weakening the corona. This leads to three different operating regimes; namely, for positions that favor ion recapture, charging is limited and current increases with wind as in the classical scaling; for positions that favor ion transport by the wind, the system charges negatively and the current decreases with wind; for the later configuration, as wind increases, the current can vanish and the system potential saturates. The results from this work demonstrate that classical scaling laws of corona discharge in wind do not necessarily apply for isolated electrodes and illustrate the feasibility of using a glow corona in wind for controlled charging of a floating body.

Plain Language Summary In the enhanced fields in thunderstorms, pointed objects such as towers, trees, wind turbine blades, or aircraft produce corona discharges. Corona discharges can also be produced in laboratory setups using sharp electrodes. In the presence of wind, the discharge is strengthened and the current increases as the wind disperses the ions that were locally reducing the magnitude of the electric field. This is a well-accepted phenomenon that appears when the electrode setup is grounded. This paper explores what happens when the electrodes are electrically isolated rather than grounded, of relevance for aircraft and some wind turbine blades. It is shown, through a wind tunnel campaign and numerical simulation, that in this case the structure becomes electrically charged due to the evacuation of ions and this effect acts to weaken the corona discharge. The results from this work demonstrate that, for electrically isolated electrodes, the corona current can actually decrease with wind and illustrate the feasibility of using corona discharge in wind to charge a floating structure such as an aircraft.

1. Introduction

Corona discharges can be initiated by thunderstorm electric fields at the tips of pointed objects such as towers, trees, wind turbine blades, or aircraft (Mokrov et al., 2013). These coronae produce space charge layers that influence the spatial distribution of the electric fields and as a result can influence the initiation and progression of leaders, impacting the probability of lightning attachment (Bazelyan et al., 2008; Rakov & Uman, 2003). In the presence of wind, the ion clouds are dispersed and their shielding effect is reduced, which qualitatively explains the observed preference of lightning attachment to rotating blades of windmills rather than to static towers (Montanya et al., 2014).

The literature on wind effects on direct current (d.c.) corona discharges is relatively abundant, with seminal work due to Chapman (1970, 1977). In this reference work, Chapman (1970) studied the magnitude of the current from a corona point discharge placed inside a wind tunnel and collected by a grounded plate. Since the wind removes the shielding ions from the coronating tip vicinity, the current was shown to be proportional to the ion speed, which reduces to a linear relationship with wind in the case of dominant wind as compared to the electrical drift. In the context of atmospheric electricity research, and motivated by

understanding the behavior of high-voltage d.c. transmission lines and grounded lightning rods in thunderstorm fields, many efforts have followed, including simulations (Bazelyan et al., 2009; Becerra, 2013; Maruvada, 2014; Mokrov et al., 2013; Nguyen et al., 2017) and field campaigns (D'Alessandro, 2009). All of these efforts contemplate earthed structures exposed to high atmospheric fields and demonstrate that, in the high-speed wind regime, the current indeed increases linearly with the wind. In addition, a number of technological applications involving corona discharge in flowing gas present similar physics, including plasma reactors, ozone generators, electrostatic precipitators, electrostatic dischargers of aerosol particles, ion drag pumps, or electroaerodynamic propulsion (Antao et al., 2009; Jaworek & Krupa, 1996; Neimarlija et al., 2009; Stuetzer, 1960; Xu et al., 2018; Yamamoto et al., 1988).

There are, however, a number of problems that are not directly addressed by those experimental and theoretical works, and that is the case of electrically isolated or floating electrode configurations. Note that in this work, the terms "isolated" and "floating" refer to electrically isolated systems, as compared to grounded configurations, regardless of the physical disposition. From the atmospheric electricity perspective, isolated electrode configurations appear when considering corona discharges at sharp extremities in aircraft, helicopter blade tips, and isolated wind turbine blade tips (Montanya et al., 2014; Moore et al., 1991; Vonnegut & Little, 1965). In addition, several studies have explored artificial charging of aircraft through charge emission, possibly using corona discharges (Jones, 1990; Stimmel et al., 1946; Waddel et al., 1946) and with several objectives in mind: from calibrating electric field mills onboard of research aircraft for the measurement of atmospheric potentials, to studying autogenous charging of an aircraft in any weather. More recent work by Guerra-Garcia et al. (2018) and Pavan et al. (2020) has proposed that artificially charging an aircraft to negative values could be used to reduce the risk of an aircraft-initiated lightning strike.

In this work, a wind tunnel experimental campaign is conducted in order to establish the dependencies of corona current with wind, when the electrode system is isolated, and to quantify the feasibility of using corona discharge in wind for charging. A numerical model is also constructed that facilitates interpretation of the experimental data and clarifies some of the details of the competing effects of the ion transport between wind and electrostatic attraction. Only the case of positive glow corona discharge is considered, since the ultimate objective was to achieve negative charging of an isolated object (Pavan et al., 2020). The paper is organized as follows: Section 2 describes the wind tunnel campaign and theoretical methods used; section 3 discusses the experimental and numerical results; finally, the main findings of this work are summarized in section 4.

2. Electrically Isolated Electrode Configuration

Motivated by the desire of achieving controlled charging of an aircraft in flight using a corona discharge, the electrode configuration selected is an idealized 2-D version of a metallic aircraft wing with a very thin corona wire stretched span-wise parallel to its surface. The high-voltage terminal of a floating d.c. power supply (Matsusada RB60-30P), of the positive polarity, is connected to the wire (acting as the anode generating the positive corona), and the low-voltage terminal is connected to the wing (acting as the cathode). The power supply was operated with batteries to ensure electrical isolation from the laboratory grid and was physically placed on the floor and electrically insulated from it using teflon blocks. The wing had a chord of 14 cm, a thickness of 2 cm, and a wing span of 101 cm. The wire had a diameter of 0.2 mm and the same length as the wing and could be positioned at various locations.

A schematic of the geometry of the wing cross section is shown in Figure 1, and the positions of the wire tested (in wing axes) are detailed in Table 1. Positions 1–7 are representative of locations close to the trailing edge, which favor convective transport of the ions by the wind; Position 8 is the most similar configuration to a wire-to-plate setup (for comparison with classical work by Lowke & D'Alessandro, 2003, for geometry effects and Chapman, 1970, for wind effects); and Positions 9–11 are representative of locations close to the leading edge of the wing, which favor ion recapture by the wing.

2.1. Wind Tunnel Campaign

The wing-wire assembly was supported by a corrugated ceramic standoff rated for 70 kV isolation and placed inside the Massachusetts Institute of Technology (MIT) Wright Brothers Wind Tunnel (WBWT). The WBWT has an elliptical test section of 3 m × 2.3 m and was operated at wind speeds up to 50 m/s. This maximum

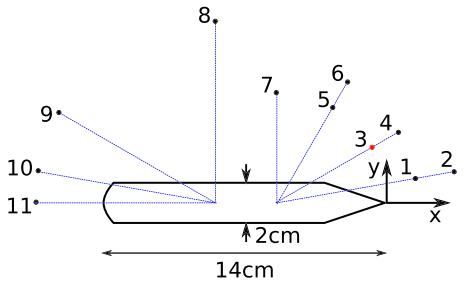

Figure 1. Wing geometry and wire positions tested. All dimensions are in cm, the figure is to-scale, and the wire positions in *x*-*y* coordinates are specified in Table 1.

wind speed was chosen since, for configurations close to the trailing edge, a saturation regime was reached beyond which further increasing the wind had no effect. This saturation level could be raised by increasing the power supply voltage, but this was not pursued to avoid spurious breakdown and leakage effects. A schematic and photograph of the full setup are shown in Figure 2.

The potential reached by the wing (to about −40 kV) was measured via a voltage divider, with resistors of 10 GΩ and 10 MΩ in series. The corona current was measured by the calibrated output current measurement of the power supply. The corona discharge was video recorded using a ultraviolet (UV)-sensitive camera (CoronaFinder) mounted on a digital camera (Sony DSC-RX10M2), the visualization system was physically placed outside the wind tunnel. The frame rate was set to 30 frames per second. The spatial resolution of the images was 1 mm/pixel. For each configuration (wire position, power supply amplitude level, and wind speed) around 1 min of operation was video recorded, ensuring steady state was reached.

2.2. Numerical Model

2.2.1. Governing Equations and Boundary Conditions

Under the conditions in the experiment, the corona discharge observed was always of the glow type, defined by Trinh (1995) as *a thin, luminous layer immediately adjacent to the anode, where intense ionization activity takes place*. Due to this disparity in length scales, glow coronae can be modeled by incorporating the thin ionization region as a boundary condition and solving only for transport. For the positive glow corona, only positive ions are accounted for since electrons are absorbed by the anode, and negative ions can be neglected considering electrons only exist in regions where the field is too high for attachment to take place (Morrow, 1997). Using this model, the steady state equations to be solved are the current conservation equation and Poisson equation:

$$\nabla \cdot [\rho(\mu\delta\vec{E} + \vec{w})] = 0, \tag{1}$$

$$\nabla \cdot \vec{E} = \frac{\rho}{\epsilon_0} \quad \text{or} \quad \nabla^2\phi = -\frac{\rho}{\epsilon_0}, \tag{2}$$

where ϵ_0 is the permittivity of vacuum, ρ is the net charge density in this case due to the positive ions alone, $\vec{E}$ is the local electric field, and ϕ is the electrostatic potential. The local wind velocity vector, $\vec{w}$, is precalculated for the geometry shown in Figure 1 and with the incident wind in the x direction, assuming incompressible and irrotational flow (neglecting viscous effects and electric wind). An example of the wind streamlines around the airfoil and wire is shown in Figure 3. The ion mobility for air at atmospheric pressure, μ, is taken in the range $1.5 \cdot 10^{-4} - 2.2 \cdot 10^{-4}$ $m^2 V^{-1} s^{-1}$ to account for variations with humidity (Tyndall & Grindley, 1926). The scaling with pressure is explicitly accounted for through the mobility dependency $\propto \delta^{-1}$, where $\delta = N/N_0$ is the relative air density (gas number density at conditions of interest over gas number density for standard atmospheric pressure air).

The boundary conditions for the electrostatic potential are the wing potential V_{wing}, and the wire potential $V_{wire} = V_{wing} + \Delta V$, where ΔV is the fixed bias applied to the floating power supply, which can be regulated from 10 to 20 kV. The potential is made zero on a relatively distant surface (of radius 45 cm from the center of

Table 1
Relative Position of Coronating Wire With Respect to Wing

Position	1	2	3	4	5	6	7	8	9	10	11
x coordinate	1.4	3.4	−0.7	0.6	−2.7	−2.0	−5.5	−8.5	−16.0	−17.0	−18.0
y coordinate	1.2	1.6	2.7	3.5	4.8	6.1	5.5	9.0	4.5	1.6	0.0

Note. All dimensions are in cm.

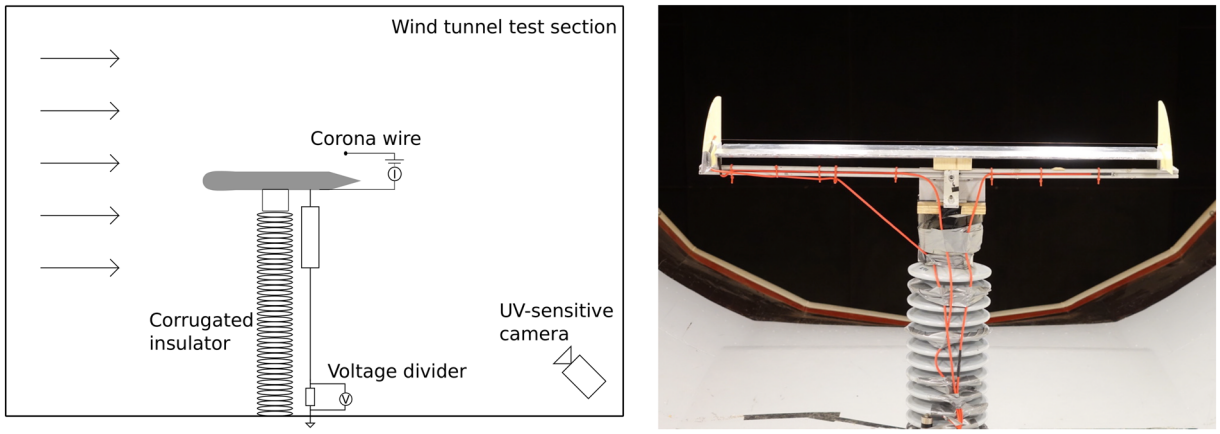

Figure 2. Experimental setup. (left) Schematic of experimental assembly inside the wind tunnel and (right) photograph of isolated wing-wire electrode system. The winglet elements serve as insulating holders for the corona wire.

the domain, see Figure 4) since for the steady state solution ions stay in the vicinity of the wing-wire system, as will be discussed.

The wing potential V_{wing} is actually unknown a priori, so an additional constraint is needed. This condition can be understood by considering the transient prior to the wing settling at its steady state potential: Ions are emitted by the wire, some are blown away by the wind and some are attracted by the wing, as it acts as the cathode of the electrode system. Since some ions are convected away, the wing charges negatively in response, so more positive ions are attracted by it and a smaller fraction of the ion population is able to escape its influence. This process continues until, in steady state, all the ions are attracted back to the wing, and the escaping ion current vanishes. Based on this transient evolution, the wing potential is iteratively reduced until no ions escape the attraction of the wing. At this point, assuming no other charging source is present, the potential of the wing has been found.

The boundary conditions for the charge density are zero charge in a distant virtual cathode surrounding the wing-wire electrode system and a charge emission condition on the wire, which is a modification to the widely used Kaptzov (1947) condition to account for the influence of the space charge, as described in section 2.2.2. As discussed in detail by Nguyen et al. (2017), the combination of wind and field effects causes the active ionization zone (or coronating surface) to occupy only a fraction of the wire perimeter. Outside this sector, no ionization occurs and the charge density is set to zero.

The partial differential Equations 1 and 2 with the relevant boundary conditions are solved in nondimensional form, using the following reference values: E_0 for the electric field, μE_0 for the velocity, the wire radius a for the length scale, and $\varepsilon_0 E_0/a$ for the charge density. E_0 is the breakdown field in standard atmospheric pressure air, defined as the field at which attachment and ionization are balanced (about $3 \cdot 10^6$ V/m).

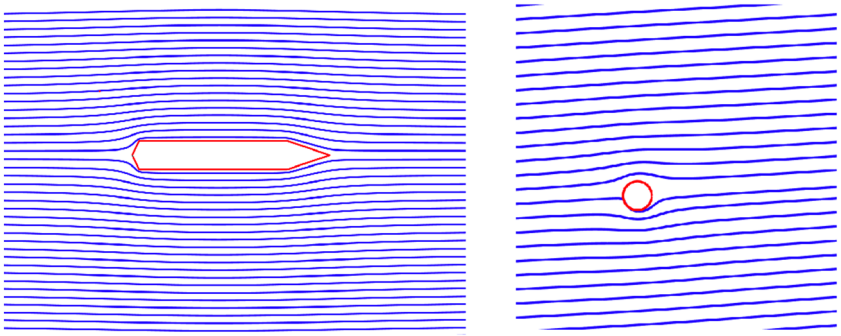

Figure 3. Wind streamlines around the airfoil (left) and a zoom in for wire Position 9 (right).

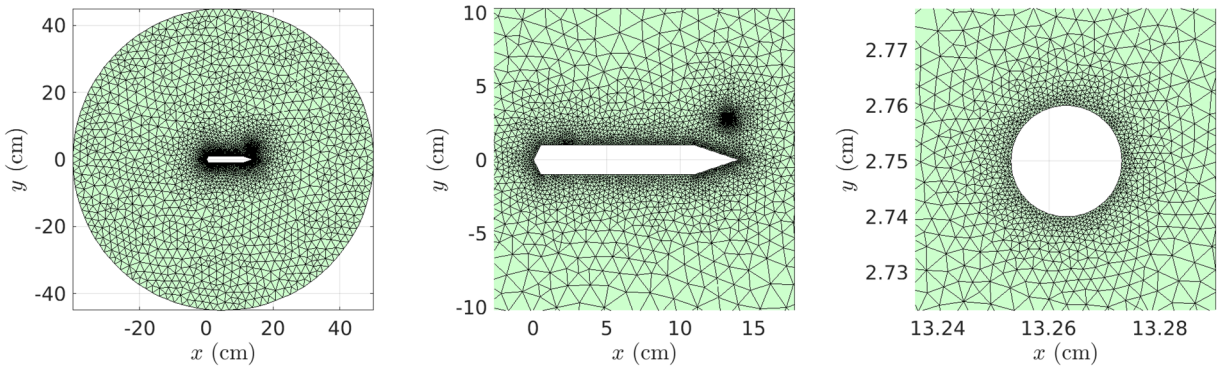

Figure 4. Computational domain and finite element mesh, with a close-up view of the mesh near the airfoil-wire system and wire.

2.2.2. The Peek Integral Electron Multiplication Condition

It is generally assumed that the electric field on a coronating electrode is close to the Peek value, which for a cylindrical wire is given in Mokrov et al. (2013) and Lowke and D'Alessandro (2003) as

$$E_P = E_0\delta\left(1+\frac{c}{\sqrt{a\delta}}\right), \tag{3}$$

where air has been assumed, a is the radius of the wire in meters, a is the relative air density, and c is an empirical dimensional constant of value $c = 0.03\,\mathrm{m}^{1/2}$. This relation has been experimentally verified at corona onset by Peek (1929) and can be derived from the general breakdown criterion:

$$\int_a^{s_0} \alpha' ds = N_e, \tag{4}$$

where α' is the net ionization coefficient, s is distance from the wire center along the local electric field line, and N_e is the number of electrons created by an avalanche that starts at the surface where the field equals the breakdown value, $E_0\delta$, ($s = s_0$) and ends on the wire ($s = a$). Indeed, for cylindrical geometry, Lowke and D'Alessandro (2003) show that Equation 3 can be exactly obtained from Equation 4 when assuming a quadratic function for the net ionization coefficient as a function of E/N and using the electric field solution to Laplace's equation (no space charge), $E(s) = E_P a/s$. Following a similar derivation but using a linear approximation to the net ionization coefficient (Lowke & D'Alessandro, 2003 propose that it is a fair approximation over a larger range of E/N), that is,

$$\frac{\alpha'}{N} = A\left(\frac{E}{N}-\frac{E_0}{N_0}\right), \tag{5}$$

the critical number of electrons, N_e, can be chosen to approximately recover Equation 3 at onset (no space charge). After nondimensionalization, it becomes

$$\int_1^{\xi_0} (e(\xi)-\delta)d\xi = R \approx \frac{0.03^2}{2a(\mathrm{m})} \approx \frac{0.413}{a(\mathrm{mm})}, \tag{6}$$

with $\xi = s/a$ is the nondimensional distance, e the nondimensional electric field, and ξ_0 the nondimensional distance from the wire at which the local electric field e is equal to the breakdown value δ. In practice, in order to avoid chattering in the determination of the coronating sector, a small tolerance is allowed in the imposed value of R, $\Delta R = \pm 5\cdot 10^{-3}$ (nondimensional, for the selected $a = 0.1$ mm).

From the above description, it can be seen that Equation 3 is most appropriate for conditions close to corona onset, but it ignores the field distortions due to space charge, which increase as the corona current increases (Liu & Becerra, 2016, 2017); in particular, the surface field can eventually be reduced to close to $E = \delta E_0$, below that given by Equation 3. For this reason, Equation 6 is used in this work instead, which allows accounting for the ion-induced field. By using the Peek integral formulation, the extinction/

intensification characteristics of the discharge, as influenced by the space charge removal by the wind and the electrode system becoming negative with respect to the environment, are revealed.

2.2.3. Computational Methods

The solution method of the partial differential equations with the given boundary conditions requires a nested iterative solution scheme: (i) Starting with an initial guess of the wing potential, the wire charge density distribution is calculated from the Peek integral electron multiplication condition, Equation 6, by using an iterative method described by Nguyen et al. (2017); (ii) having calculated the wire charge density distribution, the wing potential is determined by imposing the condition that all ions that are emitted are captured by the wing. Steps (i) and (ii) are repeated until both the Peek integral electron multiplication condition and the charge capture condition are satisfied simultaneously. In this paper, the hybridized discontinuous Galerkin method of Nguyen et al. (2009) is used for the numerical discretization of the partial differential equations. Figure 4 shows the computational domain used as well as the finite element mesh composed of isoparametric elements. The mesh is refined near the airfoil and the wire surface to properly resolve the ion density and electric field gradients.

3. Results and Discussion

3.1. Charging-Dominated Regime

The first set of experiments and simulations considers positions of the wire close to the trailing edge of the airfoil (Positions 1–7 in Figure 1), which favor the convective transport of the ions by the wind. Representative photographs of the glow corona for these wire positions as a function of the incident wind speed are shown in Figure 5. It is evident from these images that there is a deviation from the behavior reported by Chapman (1970, 1977) for grounded electrode setups: As the wind speed increases, the corona becomes less luminous and is close to extinction at the highest wind speeds tested.

The decrease in corona luminosity with wind can be explained by the excursion of the electrode system toward negative values. Figure 6 shows that, for positions close to the wing's trailing edge, increasing wind leads to more negative charging as higher wind speed will require a more negative wing potential to attract the ions back. The experimental and numerical wing potential show good qualitative and reasonable quantitative agreement. The model captures the trends observed experimentally: The wing potential increases (in magnitude) for increasing wind speed up to a saturation level, beyond which increasing the wind speed has very little effect on lowering the wing potential.

From these results, it can also be appreciated that the position of the corona-emitting wire relative to the wing has a significant impact on the charging of the airfoil. The best position from the set of positions tested in terms of charging is predicted to be, both theoretically and experimentally, Position 3. Note that the real optimum can potentially be found using the numerical model. There is a trade-off regarding distance: If the wire is very near, ions are easily captured, with no need for a high negative wing potential; if they are very far, the corona weakens too much. In addition, locations further back toward the trailing edge lead to more charging, since ion escape is facilitated.

The excursion to negative potentials is accompanied by a decrease in the current with wind speed as the potential on the corona emitter, while biased positive with respect to the wing, becomes increasingly negative with respect to space (Figures 7 and 8). This reduces the electric field on the anode, and hence, the corona becomes *weaker*: lower luminosity and lower current. Eventually, the field at the coronating anode may weaken to the point where ionization can no longer be sustained. When this happens, the corona extinguishes (the current goes to zero), and any further increase in wind speed will not affect the charge accumulated on the body, or its potential, reaching the saturation region.

The weakening of the corona can be better appreciated from the *visualization* of the ion cloud calculated with the numerical model (Figure 7) (case of Position 3, power supply bias at 13 kV). With increasing wind speed, the space charge region shrinks and finally disappears at high enough wind speed (close to 40 m/s in this case), which correlates with the similar reduction of the corona current and luminosity observed. It is also interesting to observe that the coronating segment occupies only a fraction of the wire, as a result of the electrostatics of the wire-wing configuration but also the shielding effect of the intense space charge between the wing and the wire. This observation emphasizes the usefulness of including space charge

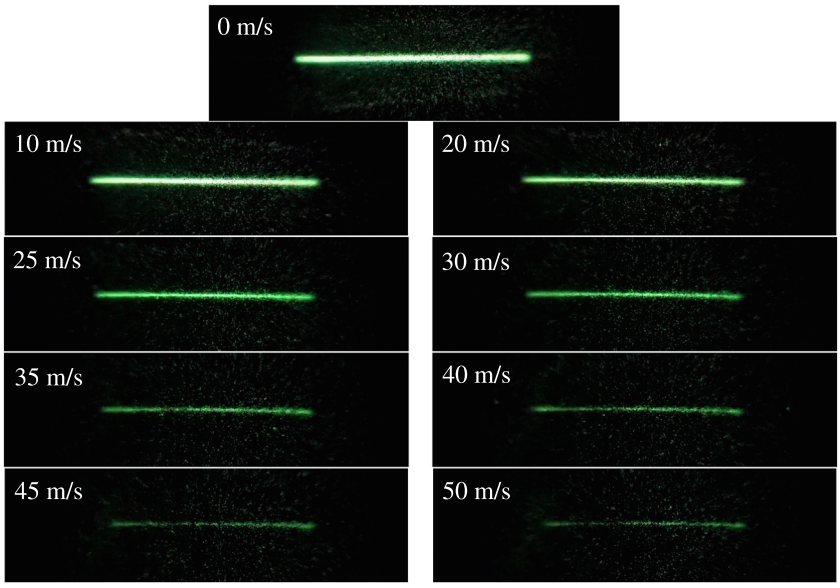

Figure 5. Dependency of corona luminosity (UV-sensitive camera) with wind speed in the charging-dominated regime. The higher the wind speed, the less luminous the corona. Images correspond to Wire Position 3 and 13 kV applied voltage between wire and wing.

effects in the corona boundary condition (Equation 4 instead of Equation 3). For these same cases, the computed electrostatic potential is shown in Figure 8 with the ion trajectories, including wind and electric drift, superimposed in black.

Note that in the experiment the corona does not totally extinguish (although it becomes very weak) (Figure 5). This is in part because of a finite leakage current through the voltage divider and also possibly because any extinction might be followed quickly by a reignition that is not captured by the d.c. measurements taken. This second loop of current becomes important for the low-current cases close to corona extinction (e.g., the leakage current for a 10 kV voltage difference across a 10 GΩ resistor is 1 μA).

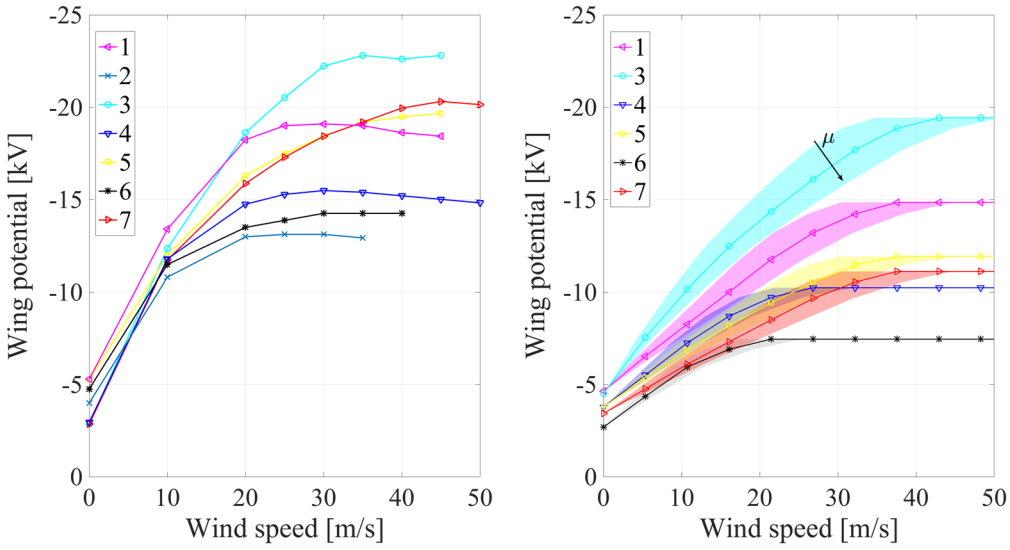

Figure 6. Wing potential as a function of wind speed in the charging-dominated regime showing the effect of different wire positions close to the wing's trailing edge with a power supply voltage of 13 kV. (left) Experimental data and (right) results of numerical model with bands around each baseline case to account for the variability of ion mobility with humidity.

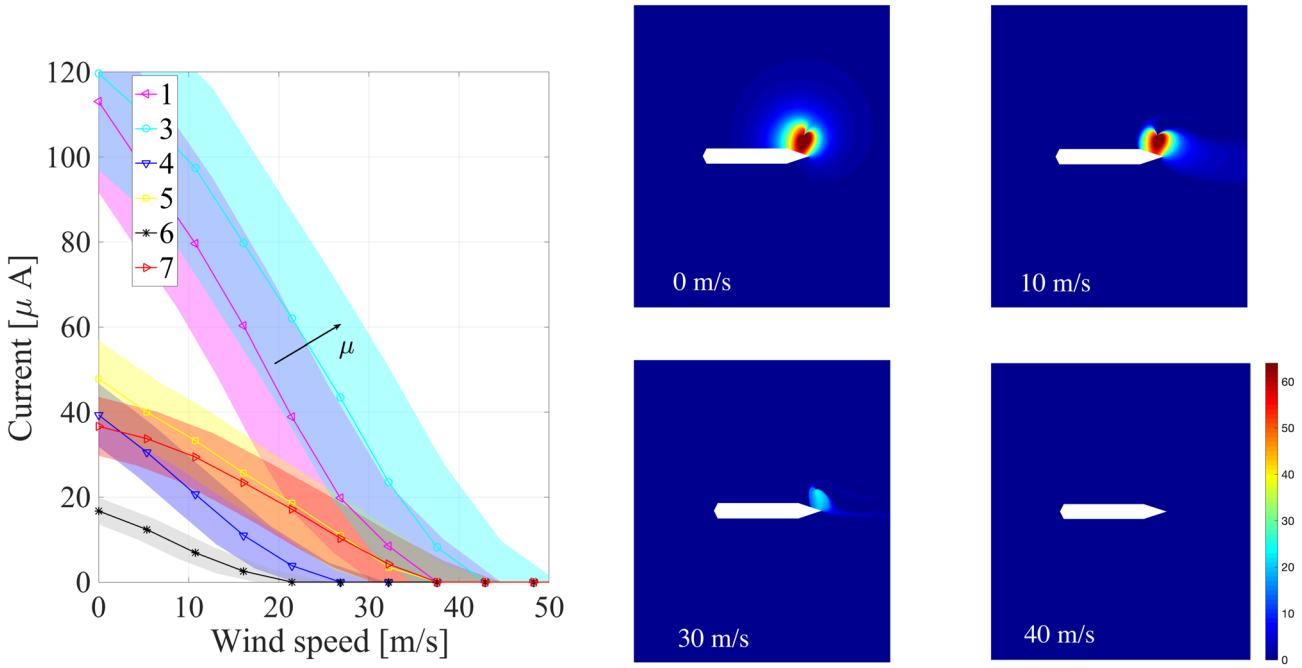

Figure 7. Numerical results for different wire positions close to the wing's trailing edge (charging-dominated regime) and fixed power supply voltage of 13 kV. (left) Corona current as a function of wind speed, the bands around each baseline case account for the variability of ion mobility with humidity. (right) Space charge density in $\mu C/m^3$ for Wire Position 3 and increasing wind.

Finally, the effects of ion mobility are also of interest. Below saturation, increasing mobility facilitates ion retrieval due to the wing potential, so a lower negative potential is sufficient to balance the wind drag. However, when saturation is reached because ion emission stops, this effect disappears, and mobility changes do not modify the potential. This observation also applies to the effect of relative air density. While the simulations have been performed for $\delta = 1$, for comparison to the experiments, mobility scales with δ^{-1} and the Peek field, to first order, scales with δ. For $\delta < 1$ (e.g., an aircraft in flight), mobility is increased and the onset field is decreased, achieving saturation at higher wind speeds and requiring lower applied voltages.

In summary, for the charging-dominated scenario, two distinct regimes can be distinguished: a low-wind regime, where the negative body potential increases more or less linearly with wind, and the corona current is nonzero, but decreasing with wind; and a high wind saturation regime, with zero current and a limiting body potential. For a given wind speed, this saturation can be overcome by increasing the power supply bias. Figure 9 shows the effect of varying the power supply bias, in the range 13–18.7 kV, for Wire Position 3. It is worth noting that both the initial slope of wing potential versus wind speed and the wing saturation potential (magnitude) increase with ΔV.

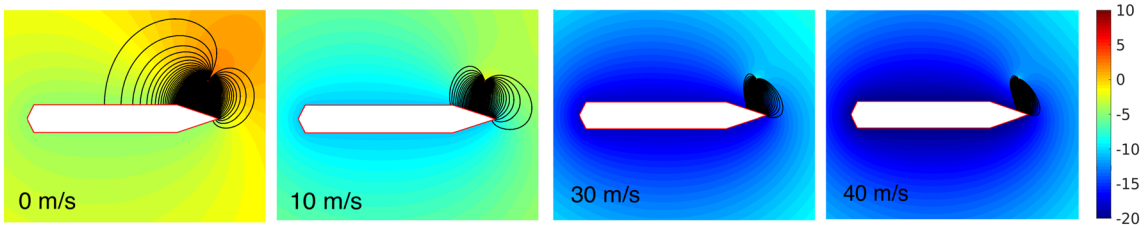

Figure 8. Electrostatic potential in kV for Wire Position 3 and power supply voltage of 13 kV. Effect of gradually increasing wind in a case showing charging-dominated behavior. Ion trajectories are shown in black.

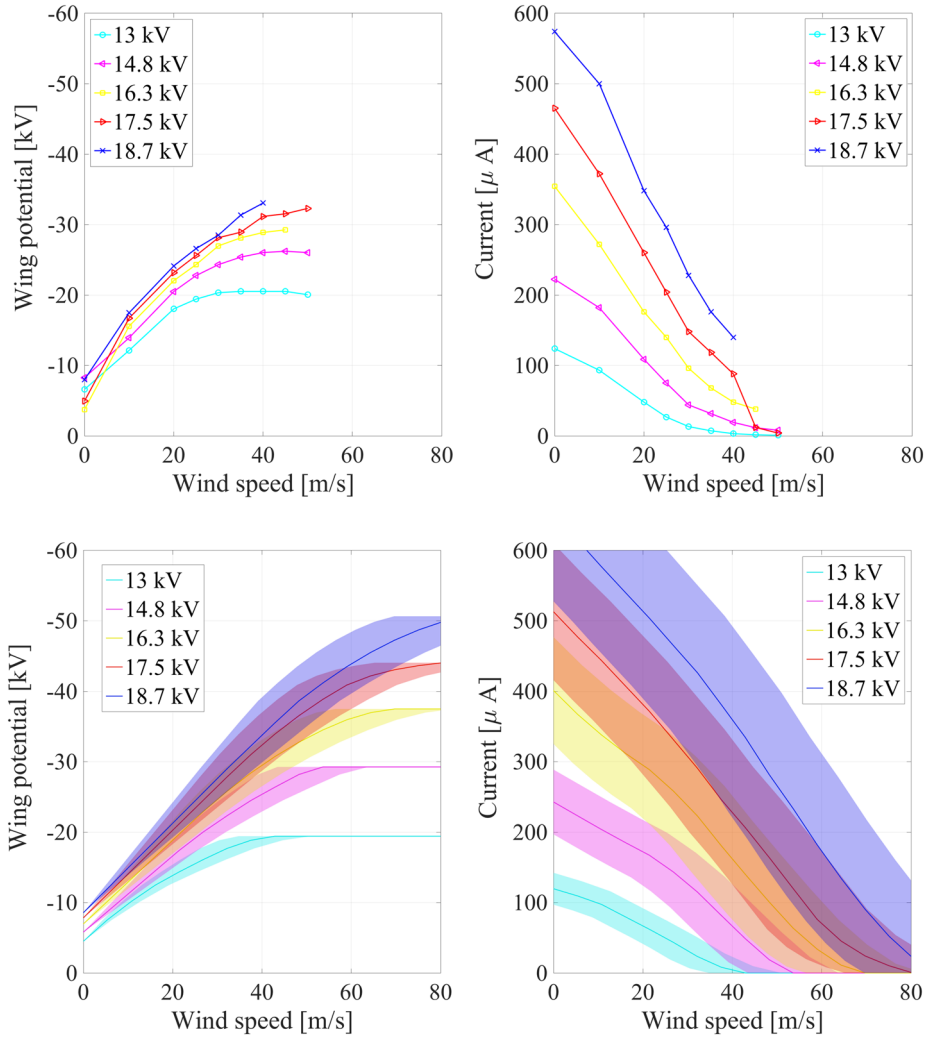

Figure 9. Experimental (top graphs) and numerical (bottom graphs) results of wing potential and corona current, as a function of wind speed, for Wire Position 3 and varying the bias voltage between 13 and 18.7 kV. The bands around each baseline case for the model results account for the variability of ion mobility with humidity.

3.2. Transition to Classical Behavior

Since the level of charging is strongly dependent on the specific geometry, the question arises whether a Chapman-like behavior could also be obtained for an isolated body. To test this, the wire was moved to the leading edge of the airfoil (Positions 9-11), facilitating ion capture even at low wing potentials.

As shown in Figure 10, by moving the wire to the leading edge, the current behavior changes drastically and lower levels of charging are obtained. For Positions 10 and 11 the current actually increases with wind, and for Position 9, the current first increases, reaches a maximum, and then decreases with the wind, marking the transition regime between classical and charging-dominated behavior. In this case, the direct effect of wind, that is, removal of the shielding ion space charge, takes precedence over the indirect effect of the negative overall potential, and the current increases initially with wind speed. Nevertheless, at some wind speed, sufficient charging is imposed to reverse the trend and reach the eventual zero-current saturation condition.

The transition can be *visualized* using the computed evolution of the ion cloud (Figure 11). It is clear that when increasing the wind speed from 0 to 10 m/s, the corona gets stronger since the wind removes part of the shielding effect. This is consistent with a current increasing with the wind. Beyond this point, the indirect effect of the wing charging takes over and the corona starts to get *weaker* until extinction at around 30 m/s.

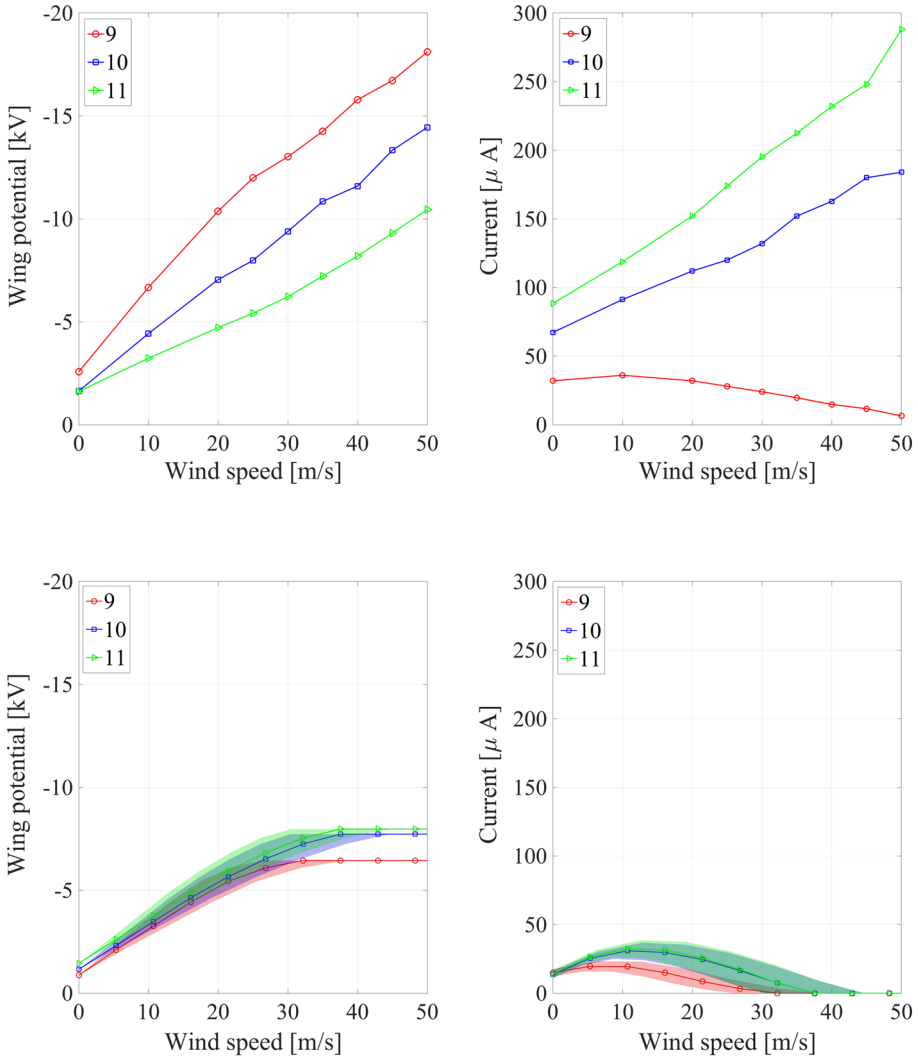

Figure 10. Transition from classical to charging-dominated behavior. Experimental (top graphs) and numerical (bottom graphs) results of wing potential and corona current, as a function of wind speed, for different wire positions close to the wing's leading edge and fixed power supply voltage of 13 kV. The bands around each baseline case for the model results account for the variability of ion mobility with humidity.

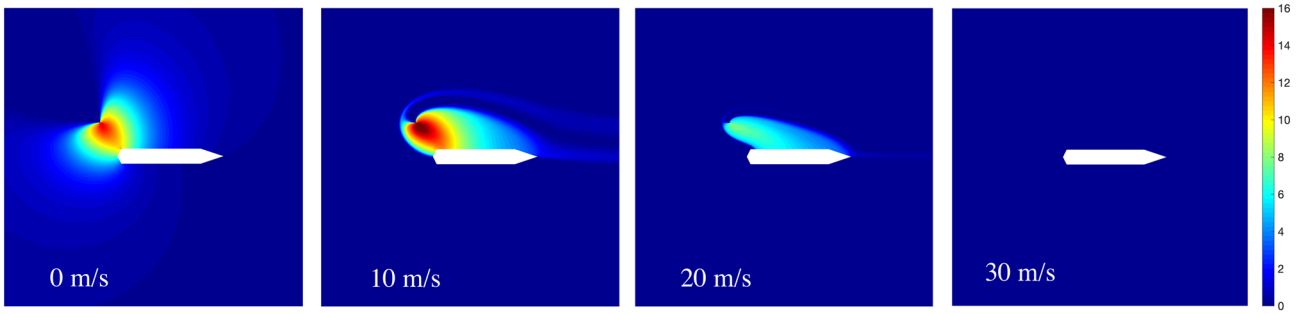

Figure 11. Space charge density in $\mu C/m^3$ for Wire Position 9 and power supply voltage of 13 kV. Effect of gradually increasing wind in a case showing transition from classical to charging-dominated behavior: left to right, 0 to 30 m/s in 10 m/s increments.

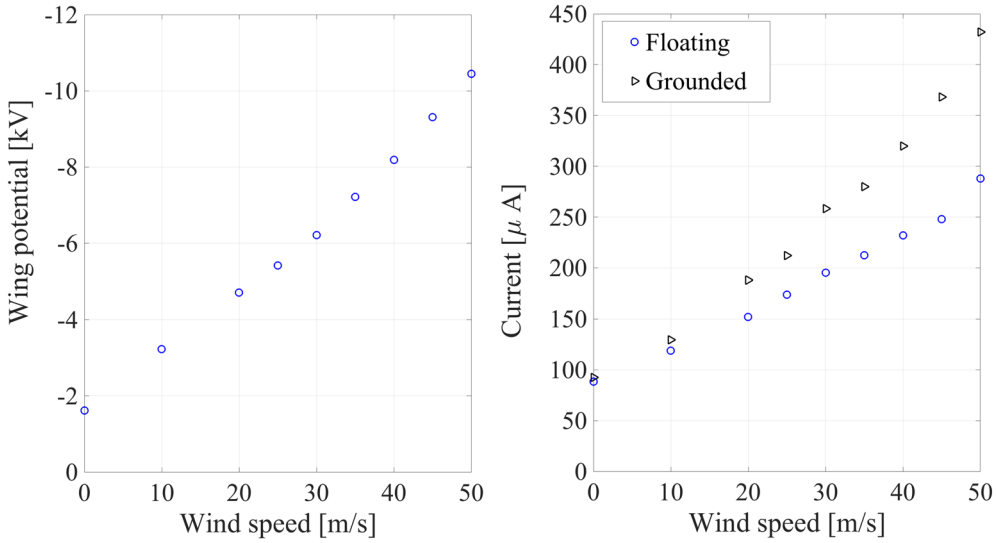

Figure 12. Comparing of isolated versus grounded wing for case of floating electrodes exhibiting classical behavior. Experimental results of wing potential and corona current, as a function of wind speed, for Wire Position 11 (leading edge) and power supply bias of 13 kV.

The model captures the transition regime of interest (Wire Position 9), but the agreement between experimental and calculated currents is poor for Wire Locations 10 and 11 near the leading edge of the wing (Figure 10). The main sources of discrepancy for these locations are (i) the effect of the far-field boundary and wind tunnel walls and (ii) the ideal flow assumption. For Positions 10 and 11 and during the transient charging phase, the ion evacuation by the wind is limited since the wire is directly facing the leading edge of the wing; hence, charging may be dominated by ions escaping to the wind tunnel walls (as influenced by the electrostatics). The presence of the wind tunnel is not captured in the model that assumes that a sufficiently distant far-field boundary has no effect on the results (the effect of this *leakage current* is discussed by Xu et al., 2020). The pitfalls of the ideal flow assumption used in the model also become more apparent for Positions 10 and 11. At a Reynolds number of $\sim 10^5$, flow separation at the nonideal leading edge of the

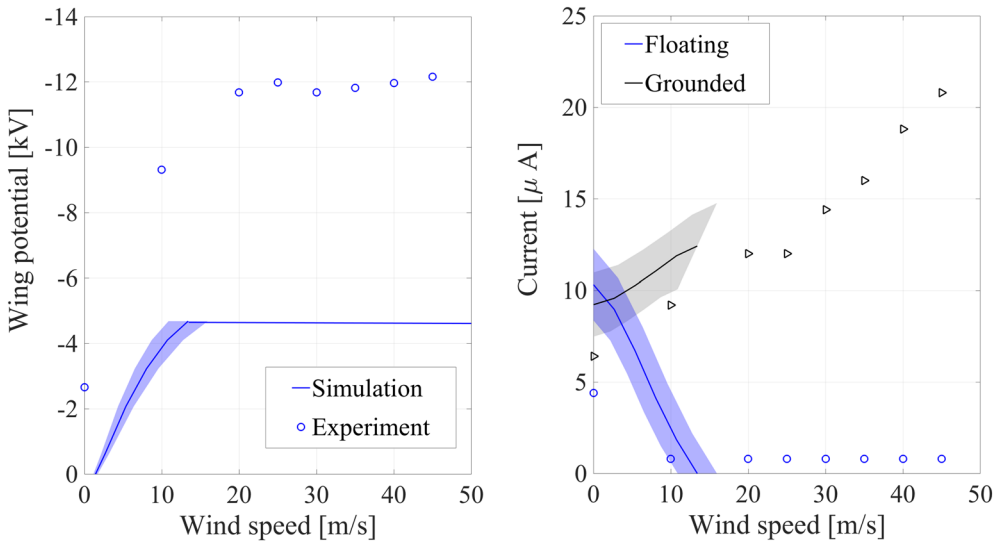

Figure 13. Comparing of isolated versus grounded wing for floating electrodes exhibiting charging-dominated behavior. Experimental (markers) and model (solid lines) results of wing potential and corona current, as a function of wind speed, for Wire Position 8 (vertical location) and power supply bias of 13 kV.

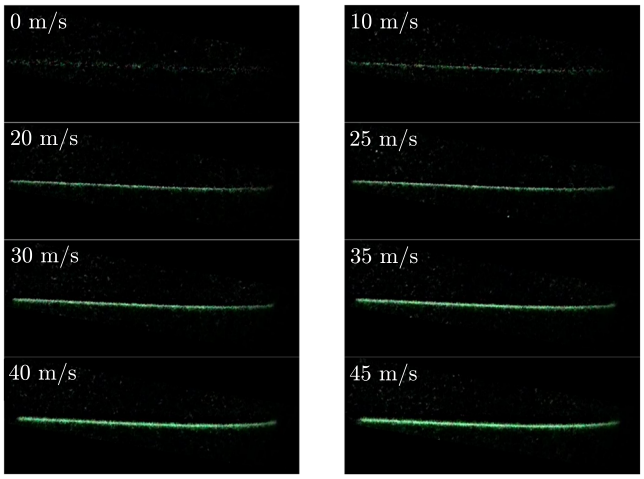

Figure 14. Dependency of corona luminosity (UV-sensitive camera) with wind speed for a grounded configuration in the classical regime. The higher the wind speed, the more luminous the corona. Images correspond to grounded wing, Wire Position 8 and 13 kV applied voltage between wire and wing.

airfoil, Figure 3, is bound to occur, whereas the model assumes the streamlines follow closely the surface of the airfoil. As a result, the model predicts high current capture and lower charging.

In summary, a third regime is observed, when moving the wire to the leading edge, in which the current first increases with wind, then reaches a maximum, and then decreases to zero.

3.3. Comparison Between Grounded and Isolated Electrodes

In order to recover the true classical corona in wind behavior, the wing needs to be grounded. Two positions of the wire were selected to compare the grounded versus isolated behavior (Positions 8 and 11). These locations were selected since they represent the most similar configuration to the classical Chapman experiments using a corona point and a collecting grounded plate (note that in this work a wire-plate configuration is used instead).

The wire position at the leading edge, Position 11, is an example of small charging levels and increasing current with wind, even when the wing is isolated. In the range tested, the reversal of the current behavior is not observed. Experimental measurement of the current for the isolated and grounded cases, as well as the floating potential measurement, is presented in Figure 12. When the wing is grounded, the current increases with wind too, but the magnitude is higher, for a given wind speed, as expected.

The vertical wire position, Position 8, when the wing is floating, is an example of the charging-dominated regime, with wing potential increasing (in magnitude) with wind speed until saturation, and current decreasing with wind until it vanishes. Experimental and theoretical results are presented in Figure 13. In this case, the magnitude of the current is low, as the wire is at the furthest distance from the wing tested. When the wing is grounded, the current with wind speed trend reverses, showing the classical increase, as expected. For completeness in the data reporting, the dependency of corona luminosity with wind in this case is show in Figure 14, as an example of a case displaying classical behavior (i.e., current and luminosity increase with wind). Note that, in general, the dependency of the luminosity with wind follows that of the current.

4. Conclusion

This paper has presented experimental and theoretical results that demonstrate that classical scaling laws of corona discharge in wind may not apply if the electrode system is not grounded. Depending on the geometry, power supply bias and wind speed, three different regimes were experimentally observed:

(1) For wire positions that favor ion transport by the wind (i.e., trailing edge positions) and low wind, the wing negative potential increases close to linearly with wind and the current and luminosity decrease with wind speed, in response to the system becoming more negative with respect to its environment.
(2) At some limiting wind speed the corona current goes to zero, marking the extinction of the charging mechanism, and the wing potential settles at its saturation value, independent of wind speed.
(3) For wire positions that favor ion recapture (i.e., leading edge positions), charging is limited and a Chapman-like behavior is recovered. In this regime, the current and luminosity increase with wind as the effect of the removal of shielding ion space charge takes precedence over the effect of charging. If the wind speed is increased enough, it is possible that the trend is again reversed and the zero-current saturation condition be reached.

The mechanisms behind each of the trends observed experimentally were clearly explained by a charge transport/electrostatic model that incorporates the effects of wind convection as well as the possibility of corona extinction due to sufficiently negative potential excursions.

The results presented in this work illustrate the feasibility of using a glow corona discharge in wind for controlled charging of an isolated body (e.g., an aircraft or a helicopter in flight) via ion emission. The charging

level achieved depends on geometry, wind speed, and biasing voltage; and in particular, there is an optimal wire-wing position that leads to the highest charging levels.

Data Availability Statement

The wind tunnel data presented in this paper, including video recordings for all experiments, can be found in the Harvard Dataverse (https://doi.org/10.7910/DVN/DNMEDE).

Acknowledgments
This work was supported by The Boeing Company through the Strategic Universities for Boeing Research and Technology Program. The authors would like to thank J. Peraire for useful discussions about the numerical solution of the equations, J. Montanya for his contributions to the experimental campaign, D. Robertson for operating the Wright Brothers Wind Tunnel, B. Shuster for the help with formatting of the figures, and W. P. Winn for his revisions to the manuscript.

References

Antao, D. S., Staack, D. A., Fridman, A., & Farouk, B. (2009). Atmospheric pressure dc corona discharges: operating regimes and potential applications. *Plasma Sources Science and Technology*, *18*(3), 35,016. https://doi.org/10.1088/0963-0252/18/3/035016

Bazelyan, E. M., Raizer, Y. P., & Aleksandrov, N. L. (2008). Corona initiated from grounded objects under thunderstorm conditions and its influence on lightning attachment. *Plasma Sources Science and Technology*, *17*(2), 24015. https://doi.org/10.1088/0963-0252/17/2/024015

Bazelyan, E. M., Raizer, Y. P., Aleksandrov, N. L., & D'Alessandro, F. (2009). Corona processes and lightning attachment: The effect of wind during thunderstorms. *Atmospheric Research*, *94*(3), 436–447. https://doi.org/10.1016/j.atmosres.2009.07.002

Becerra, M. (2013). Glow corona generation and streamer inception at the tip of grounded objects during thunderstorms: Revisited. *Journal of Physics D: Applied Physics*, *46*(13), 135,205. https://doi.org/10.1088/0022-3727/46/13/135205

Chapman, S. (1970). Corona point current in wind. *Journal of Geophysical Research*, *75*(12), 2165–2169. https://doi.org/10.1029/JC075i012p02165

Chapman, S. (1977). The magnitude of corona point discharge current. *Journal of the Atmospheric Sciences*, *34*, 1801–1809. https://doi.org/10.1175/1520-0469(1977)034<1801:TMOCPD>2.0.CO;2

D'Alessandro, F. (2009). Experimental study of the effect of wind on positive and negative corona from a sharp point in a thunderstorm. *Journal of Electrostatics*, *67*(2-3), 482–487. https://doi.org/10.1016/j.elstat.2008.12.003

Guerra-Garcia, C., Nguyen, N. C., Peraire, J., & Martinez-Sanchez, M. (2018). Charge control strategy for aircraft-triggered lightning strike risk reduction. *AIAA Journal*, *56*(5), 1988–2002. https://doi.org/10.2514/1.J056406

Jaworek, A., & Krupa, A. (1996). Corona discharge from a multipoint electrode in flowing air. *Journal of Electrostatics*, *38*(3), 187–197. https://doi.org/10.1016/S0304-3886(96)00023-X

Jones, J. J. (1990). Electric charge acquired by airplanes penetrating thunderstorms. *Journal of Geophysical Research*, *95*(10), 16,589–16,600. https://doi.org/10.1029/JD095iD10p16589

Kaptzov, N. A. (1947). *Electricheskiye Yavleniya v Gazakh i Vacuume*. Moscow: OGIZ.

Liu, L., & Becerra, M. (2016). On the transition from stable positive glow corona to streamers. *Journal of Physics D: Applied Physics*, *49*(22), 225,202. https://doi.org/10.1088/0022-3727/49/22/225202

Liu, L., & Becerra, M. (2017). An efficient model to simulate stable glow corona discharges and their transition into streamers. *Journal of Physics D: Applied Physics*, *50*(10), 105,204. https://doi.org/10.1088/1361-6463/aa5a34

Lowke, J. J., & D'Alessandro, F. (2003). Onset corona fields and electrical breakdown criteria. *Journal of Physics D: Applied Physics*, *36*(21), 2673–2682. https://doi.org/10.1088/0022-3727/36/21/013

Maruvada, P. S. (2014). Influence of wind on the electric field and ion current environment of HVDC transmission lines. *IEEE Transactions on Power Delivery*, *29*(6), 2561–2569. https://doi.org/10.1109/TPWRD.2014.2302373

Mokrov, M. S., Raizer, Y. P., & Bazelyan, E. M. (2013). Development of a positive corona from a long grounded wire in a growing thunderstorm field. *Journal of Physics D: Applied Physics*, *46*(45), 455202 (14pp). https://doi.org/10.1088/0022-3727/46/45/455202

Montanya, J., van der Velde, O., & Williams, E. R. (2014). Lightning discharges produced by wind turbines. *Journal of Geophysical Research: Atmospheres*, *119*, 1455–1462. https://doi.org/10.1002/2013JD020225

Moore, C. B., Jones, J. J., Hunyady, S. J., Rison, W., & Winn, W. P. (1991). Electrical hazards to airborne operations: Technical Report for The Applied Research and Technology Directorate ONR N00014-87-K-0783. Retrieved from https://apps.dtic.mil/dtic/tr/fulltext/u2/a253655.pdf

Morrow, R. (1997). The theory of positive glow corona. *Journal of Physics D: Applied Physics*, *30*(22), 3099–3114. https://doi.org/10.1088/0022-3727/30/22/008

Neimarlija, N., Demirdzic, I., & Muzaferija, S. (2009). Finite volume method for calculation of electrostatic fields in electrostatic precipitators. *Journal of Electrostatics*, *67*(1), 37–47. https://doi.org/10.1016/j.elstat.2008.10.007

Nguyen, N. C., Guerra-Garcia, C., Peraire, J., & Martinez-Sanchez, M. (2017). Computational study of glow corona discharge in wind: Biased conductor. *Journal of Electrostatics*, *89*, 1–12. https://doi.org/10.1016/j.elstat.2017.06.005

Nguyen, N. C., Peraire, J., & Cockburn, B. (2009). An implicit high-order hybridizable discontinuous Galerkin method for nonlinear convection diffusion equations. *Journal of Computational Physics*, *228*(23), 8841–8855. https://doi.org/10.1016/j.jcp.2009.08.030

Pavan, C., Fontanes, P., Urbani, M., Nguyen, N. C., Martinez-Sanchez, M., Peraire, J., et al. (2020). Aircraft charging and its influence on triggered lightning. *Journal of Geophysical Research: Atmospheres*, *125*, e2019JD031245. https://doi.org/10.1029/2019JD031245

Peek, F. W. (1929). *Dielectric phenomena in high voltage engineering*. New York: McGraw Hill.

Rakov, V. A., & Uman, M. A. (2003). *Lightning physics and effects*. Cambridge: Cambridge University Press.

Stimmel, R. G., Rogers, E. H., Waterfall, F. E., & Gunn, R. (1946). Army-Navy Precipitation-Static project: Part III—Electrification of aircraft flying in precipitation areas. *Proceedings of the IRE*, *34*(4), 167–177. https://doi.org/10.1109/JRPROC.1946.234238

Stuetzer, O. M. (1960). Ion drag pumps. *Journal of Applied Physics*, *31*(1), 136–146. https://doi.org/10.1063/1.1735388

Trinh, N. G. (1995). Partial discharge XIX: Discharge in air Part I: Physical mechanisms. *IEEE Electrical Insulation Magazine*, *11*(2), 23–29. https://doi.org/10.1109/MEI.1995.1025997

Tyndall, A. M., & Grindley, G. C. (1926). The mobility of ions in air. Part I. Negative ions in moist air. *Proceedings of the Royal Society of London*, *110*, 341–364. https://doi.org/10.1098/rspa.1926.0019

Vonnegut, B., & Little, A. D. (1965). Electrical behavior of an airplane in a thunderstorm (*FAA–ADS–36*): Technical Report for Federal Aviation Agency. Retrieved from https://apps.dtic.mil/dtic/tr/fulltext/u2/614914.pdf

Waddel, R. C., Drutowski, R. C., & Blatt, W. N. (1946). Army-navy precipitation-static project: Part II—Aircraft instrumentation for precipitation-static research. *Proceedings of the IRE*, *34*(4), 161–166. https://doi.org/10.1109/JRPROC.1946.225950

Xu, H., Gomez-Vega, N., Agrawal, D. R., & Barrett, S. R. H. (2020). Higher thrust-to-power with large electrode gap spacing electroaerodynamic devices for aircraft propulsion. *Journal of Physics D: Applied Physics*, *53*(2), 025202 (11pp). https://doi.org/10.1088/1361-6463/ab4a4c

Xu, H., He, Y., Strobel, K. L., Gilmore, C. K., Kelley, S. P., Hennick, C. C., et al. (2018). Flight of an aeroplane with solid-state propulsion. *Nature Letter*, *563*, 532–539. https://doi.org/10.1038/s41586-018-0707-9

Yamamoto, T., Lawless, P. A., & Sparks, L. E. (1988). Narrow-gap point-to-plane corona with high velocity flows. *IEEE Transactions on Industry Applications*, *24*(5), 934–939. https://doi.org/10.1109/28.9001